Self-Organizing Knotted Magnetic Structures in Plasma

C. B. Smiet,[1] S. Candelaresi,[2] A. Thompson,[3] J. Swearngin,[3] J. W. Dalhuisen,[1] and D. Bouwmeester[1,3]
[1]Huygens-Kamerlingh Onnes Laboratory, Leiden University, P.O. Box 9504, 2300 RA Leiden, The Netherlands
[2]Division of Mathematics, University of Dundee, Dundee DD1 4HN, United Kingdom
[3]Department of Physics, University of California Santa Barbara, Santa Barbara, California 93106, USA
(Received 31 December 2014; published 24 August 2015)

We perform full-magnetohydrodynamics simulations on various initially helical configurations and show that they reconfigure into a state where the magnetic field lines span nested toroidal surfaces. This relaxed configuration is not a Taylor state, as is often assumed for relaxing plasma, but a state where the Lorentz force is balanced by the hydrostatic pressure, which is lowest on the central ring of the nested tori. Furthermore, the structure is characterized by a spatially slowly varying rotational transform, which leads to the formation of a few magnetic islands at rational surfaces. We then obtain analytic expressions that approximate the global structure of the quasistable linked and knotted plasma configurations that emerge, using maps from S^3 to S^2 of which the Hopf fibration is a special case. The knotted plasma configurations have a highly localized magnetic energy density and retain their structure on time scales much longer than the Alfvénic time scale.

DOI: 10.1103/PhysRevLett.115.095001 PACS numbers: 52.65.Kj, 52.55.Dy, 95.30.Qd

Understanding the types of structures in magnetic fields that occur in magnetohydrodynamics (MHD) is of fundamental importance for nuclear fusion [1,2] and astrophysics [3–6]. Helicity-constrained, unbounded excitations in plasmas are present in a wide range of scales, from underdense bubbles emitted from active galactic nuclei (∼10 kpc) [7], through magnetic structures ejected from the solar corona ($\sim 10^{5-6}$ km) [8] to the structure in fusion reactors such as the spheromak [9] and field-reversed configurations [10] (∼m), and the plasmoids in dense plasma focus experiments (∼mm) [11]. There exist many analytical solutions for the field in toroidal confinement vessels [12] and bounded domains [13], and even confinement vessels in the shape of a knot [14]. There are also analytical expressions for unbounded force-free fields [15], but no analytical expression has been found for a localized field that agrees with observed structures seen in unbounded plasmas.

Magnetic helicity, defined as $H_m = \int \mathbf{A} \cdot \mathbf{B} d^3x$, where $\mathbf{A}$ and $\mathbf{B}$ are the vector potential, respectively, the magnetic field, was recognized by Woltjer to be an invariant of an ideal plasma [16]. The identification of helicity as a linking of magnetic field lines by Moffatt [17] gave a clear topological interpretation. Given the topological nature of this invariant, Kamchatnov used the structure of the Hopf fibration to construct a topological soliton in ideal MHD [18]. Recently this work was generalized by Thompson *et al.* [19]. This structure has not been described in resistive MHD, but also there helicity and magnetic topology play an important role in constraining magnetic relaxation [12,20–23]. In order to understand the effect of helicity in resistive plasmas we simulate the time evolution of various helical initial conditions and find that each of them evolves towards an ordered state of nested toroidal magnetic surfaces.

We simulate the plasma dynamics using the PENCIL CODE [24]. With this code we solve the resistive MHD equations in dimensionless form for an isothermal plasma in a fully periodic box of volume $(2\pi l_0)^3$ (see Supplemental Material [25]). We choose as initial conditions simple configurations that are clear examples of fields containing helicity, rings of flux that are all linked and/or twisted. We start simulations with n identical magnetic flux tubes that are all linked, with n ranging from 2 to 6. The flux tubes have a magnetic field of $1\mathcal{B}_0$ at the center of the tube, a radius of $\sqrt{2}l_0$, and a Gaussian intensity profile with a characteristic width of $0.16l_0$. For the $n = 3$ configuration we also vary the twist T which indicates the number of windings of a field line around the center of the tube as it passes around the tube once, further increasing helicity. Two initial conditions are shown in Figs. 1(a) and 1(c). The velocity is initially zero everywhere and the density ρ is set to 1 uniformly in the initial condition. The kinematic viscosity and magnetic diffusivity are 2×10^{-4}, giving a magnetic Prandtl number of unity. The magnetic helicity of the initial conditions is given by $H_m = (n^2 - n)\Phi^2 + nT\Phi^2$, where Φ is the magnetic flux through a single ring (see Supplemental Material [25]).

The configurations evolve in a similar fashion, which can be divided into two regimes, reconnection and resistive decay, as shown in Figs. 1(e) and 1(f). We use Alfvénic time $t_A = 1/(2\sqrt{2}\pi l_0)$, scaled by the length of a flux tube. The tubes first contract, as this lowers the magnetic energy. This process is further detailed in the Supplemental Material [25]. The higher the initial helicity, the less energy can be lost through reconfiguration. Figure 1(g) shows the

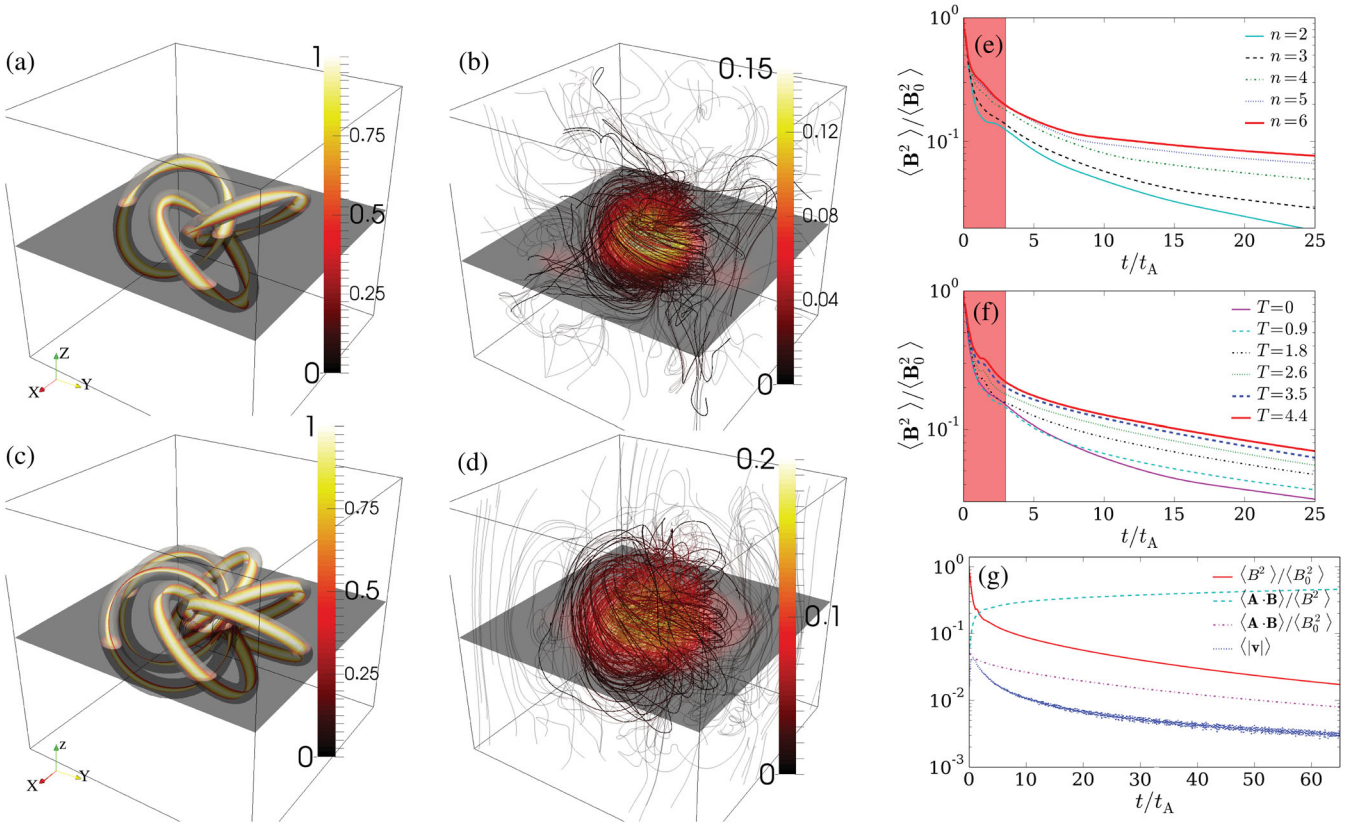

FIG. 1 (color). Simulated configurations and evolution of magnetic fields. (a),(b) Initial condition and state at $t = 22.5t_A$ for the $n = 3$ and $T = 1.8$ simulation. (c),(d) The same for the $n = 6$ and $T = 0$ simulation. In (a) and (c) a magnetic isosurface of $|\mathbf{B}| = 0.1\mathcal{B}_0$ is shown to indicate the boundary of the flux tube. In (b) and (d) the lines represent the magnetic field lines. The outer field lines are partially transparent to not obstruct the view of the central configuration. (e) Decay of magnetic energy for the simulations with $T = 0$ and n ranging from 1 to 6, and (f) the simulations with $n = 3$ and T ranging from 0 to 4.4. The shaded region indicates reconfiguration, after that resistive decay takes over. (g) The evolution of the average of the magnetic energy $\langle B^2\rangle/\langle B_0^2\rangle$, normalized helicity $\langle \mathbf{A}\cdot\mathbf{B}\rangle/\langle B^2\rangle$, helicity $\langle \mathbf{A}\cdot\mathbf{B}\rangle/\langle B_0^2\rangle$, and velocity $\langle|\mathbf{v}|\rangle$ for the simulation with $n = 3$ and $T = 1.8$.

evolution of several related quantities for the simulation with $n = 3$ and $T = 1.8$.

In order to analyze the emerging plasma configuration we take a detailed look at the simulation with $n = 3$ and $T = 1.8$ at time $t = 22.5t_A$. The magnetic energy is highly localized [Fig. 2(a)], falling off from the center. Remarkably, from the chaotic collapse of the initial condition, containing only a discrete rotational symmetry around the z axis, an ordered magnetic structure emerges that is roughly axisymmetric and where field lines span invariant tori. These are toroidal surfaces spanned by magnetic field lines and are often described in the context of toroidal fusion devices [26]. Four toroidal surfaces are shown in Fig. 2(a).

With higher initial helicity this structure appears sooner and is more pronounced. Invariant tori are observed in all simulations except the $n = 2$ simulation which was stopped at $t = 60t_A$. In the $n = 3$ and $T = 0$ simulation tori were found only after $t = 54t_A$, but in all other simulations this structure appears before $t = 22.5t_A$ and remains. Invariant tori are also observed in simulations using different helical initial conditions, such as a single twisted ring and a trefoil knotted flux tube (see Supplemental Material [25]).

The initial reconfiguration of the rings induces pressure waves traveling through the periodic simulation volume. However, these pressure waves do not significantly affect the magnetic structure. To investigate the role of pressure in the simulation we average out these waves by averaging 365 snapshots between $t = 27.5t_A$ and $t = 35.8t_A$. Figure 3(c) shows the averaged pressure, which is lowest on the magnetic axis of the structure. An ambient pressure p_∞ is therefore inherent to the structure. The force due to the pressure gradient is balanced by the Lorentz force, which makes the structure quasistable. In Figs. 3(a) and 3(b) we show the average radial component of the Lorentz F_L^r, and minus the average radial component of the pressure gradient $-\nabla P_r$ in the x, y plane passing through the center of the structure (top view of the torus).

Note that the *lowered* pressure in the structure is consistent with the virial theorem [27,28] that states that a free plasma cannot uphold an *increase* in pressure solely by internal hydromagnetic forces. The region of highest

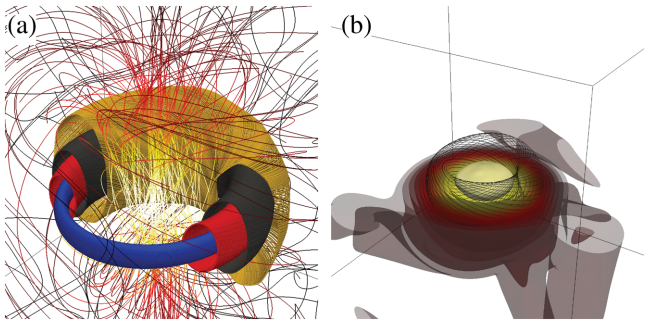

FIG. 2 (color). The simulation with $n = 3$ and $T = 1.8$ at time $t = 22.5t_A$. (a) The magnetic field contains invariant tori. Every surface is a single integral curve of the field of length $1000l_0$ colored differently for clarity. The surfaces are clipped to show the nested configuration. (b) Surfaces of constant magnetic field strength. A single torus is shown in black to indicate the scale of the magnetic structure.

magnetic field strength is near the geometrical center of the tori, where the pressure is unchanged.

The balance of magnetic and hydrostatic forces indicates that the magnetic field forms self-stable, localized structures in MHD equilibrium with ambient pressure p_∞. These equilibria feature rich dynamics such as the formation of magnetic islands at rational surfaces that are an area of intense research [26,29].

In order to investigate the nature of this equilibrium we construct a Poincaré plot of the field in Fig. 2. As seed points we choose 500 points on a line from the geometrical center of the tori and through the magnetic axis, starting on the magnetic axis and moving outward. We label this direction x^*, and the direction perpendicular to that and out of the plane of the torus we call z^*. The field lines are traced

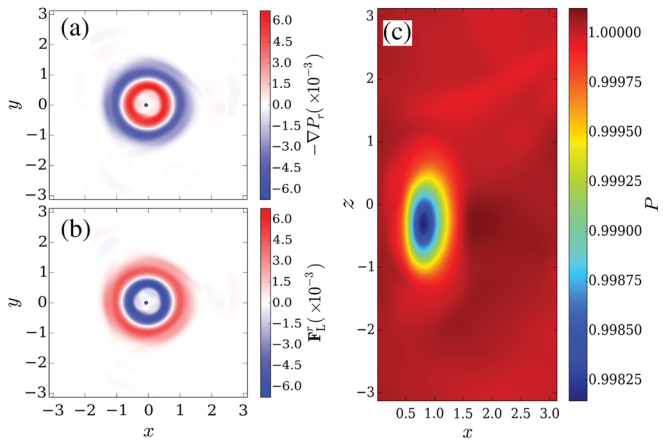

FIG. 3 (color). (a) The radial component of minus the gradient of the averaged pressure field, and (b) the radial component of the averaged Lorentz force, taken in the x, y plane (top view). The geometrical center of the tori is taken as the origin, and is marked by the blue dot. (c) The pressure field in the x, z half-plane, showing a lowered pressure in the center of the magnetic surfaces.

for a distance of $4000l_0$, and the positions where they cross the plane defined by x^* and z^* are marked. The Poincaré plot is shown in Fig. 4(a). We show the rotational transform ι [30] of the corresponding field line in Fig. 4(b) (see Supplemental Material [25] for the calculation).

As expected from [26], where the rotational transform crosses rational values, we observe magnetic islands. Lines are drawn indicating where the rotational transform crosses the values 8/9, 7/8, 6/7, and 5/6. As expected the number of islands observed is equal to the denominator of the rotational transform. Even though ι crosses a few rational surfaces, the value varies less than 10%. In a tokamak equilibrium, where the inverse of ι, the safety factor q, is

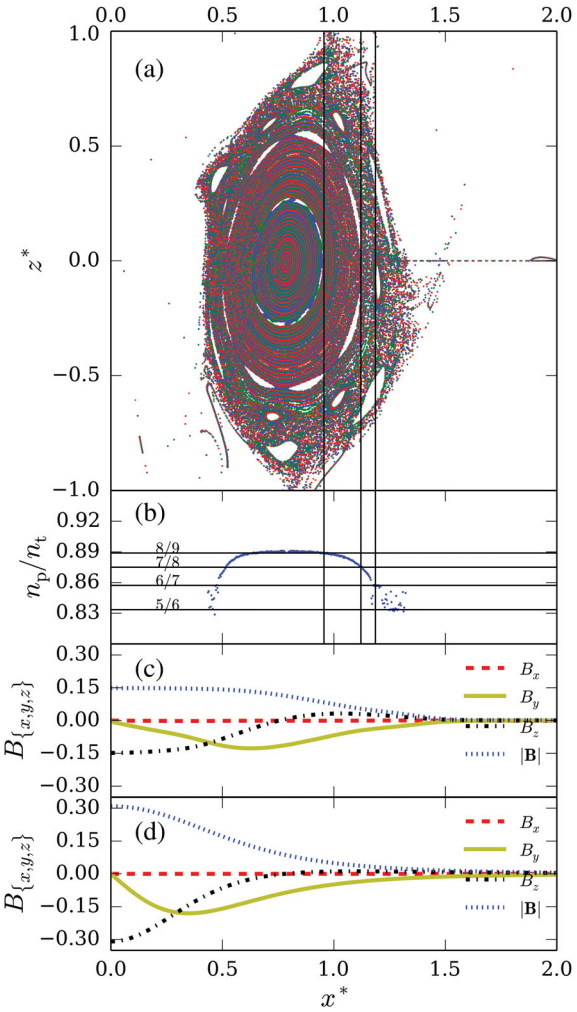

FIG. 4 (color). Poincaré plot and properties of the force-balanced toroidal structure. (a) Poincaré plot of the magnetic field. (b) The value of the rotational transform for each magnetic surface. Rational values are indicated by the labeled horizontal lines, and the positions where they cross are shown by vertical lines. (c) Value of the magnetic field strength, and the components at each position. (d) The magnetic field strength and components of the magnetic field for the analytical expression of a field with the same energy and rotational transform.

used, this value typically varies much more [31]. We note that the fact that our pressure plots result from an averaging over time implies that we cannot resolve the fine structure in the pressure, such as possible discontinuities in pressure over specific irrational Kolmogorov-Arnold-Moser surfaces as described in [32].

The magnetic field strength and the x^*, y^*, and z^* components (with y^* perpendicular to z^* and x^*) at the position of the seed points are shown in Fig. 4. The field varies continuously over the surfaces, and the magnitude is highest in the geometrical center of the structure.

The part of the magnetic field that forms toroidal magnetic surfaces is reasonably axisymmetric, and could, in principle, be approached by a solution to the Grad Shafranov equation [28]. This would, however, not capture the large part of the field outside of this ordered region. Instead we want to point out a curious resemblance between the structure of the Hopf fibrations and the fields observed here.

Non-null-homotopic maps (functions) from S^3 (hypersphere) to S^2 (sphere) such as the Hopf map [33] feature a topological structure resembling the observed plasma structures. The fibers (pre-images of points on S^2) of the map are continuous curves that lie on the surfaces of nested tori. Furthermore, every fiber is linked with every other one, with the linking number depending on the map. Through stereographic projection from S^3 to $\mathbb{R}^3$ the fiber structure of this map can be translated to a vector field in $\mathbb{R}^3$ whose integral curves are the fibers of this map (derivation in the Supplemental Material [25]). Moreover, the obtained field is smooth, continuous, divergenceless, has helicity, and the field lines lie on the surfaces of nested tori.

This curious structure was used by Kamchatnov to describe a soliton in ideal MHD, where the fluid velocity is parallel to the magnetic field everywhere [18]. Independently, Rañada used the structure of the Hopf map to construct full radiative solutions of Maxwell's equations [34,35]. Kamchatnov's solution was generalized by Sagdeev [36], and a similar extension of Rañada's fields was described by Arrayás and Trueba [37].

The analytical form of this vector field in $\mathbb{R}^3$ is given by

$$\mathbf{B} = \frac{4r_0^4\sqrt{a}}{\pi(r_0^2+r^2)^3}\begin{pmatrix} 2(\omega_2 r_0 y - \omega_1 xz) \\ -2(\omega_2 r_0 x + \omega_1 yz) \\ \omega_1(-r_0^2 + x^2 + y^2 - z^2)\end{pmatrix}. \quad (1)$$

This field is cylindrically symmetric around the z axis (see Supplemental Material [25]). It has a finite magnetic energy, as can be seen from

$$\int B^2 d^3x = a r_0^3(\omega_1^2 + \omega_2^2), \quad (2)$$

and nonzero helicity, given by

$$H_m = a r_0^4 \omega_1 \omega_2, \quad (3)$$

and like the field in the simulation it tends to zero away from the center.

In our observed structure, the fluid velocity is neither parallel nor proportional to the magnetic field, making this structure fundamentally different from the structure Kamchatnov described [18]. Nevertheless, the magnetic topology of field lines lying on nested toroidal surfaces, the magnetic energy localized in the center, the near constant rotational transform, and the direction of the magnetic field, even outside of the area that forms magnetic surfaces, all agree qualitatively with the toroidal structure described by Eq. (1). To quantify this claim we extract from the simulation the parameters ω_1, ω_2, and r_0, needed for Eq. (1) (method described in the Supplemental Material), and show that there is overall agreement.

For the simulation with $n = 3$ and $T = 1.8$ this yields values of $r_0 = 0.78$, $\omega_1 = 0.24$, and $\omega_2 = 0.27$. Parameters for the other simulations are quite similar (see Supplemental Material [25]). The analytical magnetic field is shown in Fig. 4(d) for the same positions as the extracted field in 4(c). Even though there are differences in the magnitude of the components, there is broad agreement, which is quite remarkable for a routine that only uses three independent variables that are not fit, but calculated from select parameters extracted from the simulation. As time elapses r_0 increases and ω_1/ω_2 decreases. This change is such that over $45t_A$ r_0 increases by 35% and ω_1/ω_2 decreases by 50%.

We have shown that reconnection of helical fields in resistive MHD causes the emergence of a self-stable toroidal magnetic field in force equilibrium. This equilibrium results from a balancing of magnetic forces and the pressure gradient, and has a minimum in pressure on the magnetic axis. Note that this is not a Taylor state, and the pressure profile is inverse to the pressure enforced in a Tokamak reactor. In the quasistable state there is rich dynamics such as the emergence of magnetic islands at rational surfaces.

Furthermore, we obtained an analytic expression for a magnetic field whose field lines lie on nested tori, requiring only three independent parameters. This field is a good approximation for the plasma configurations that emerge in the simulations, where a significant portion of the magnetic field lines reconfigure to lie on nested toroidal magnetic surfaces. We have observed the formation of this self-stable structure for various initial plasma configurations containing helicity. This indicates that this structure is a fundamental configuration that we predict to occur in situations where there is unbounded plasma containing helicity.

We wish to thank Marco de Baar, Hugo de Blank, Hans Goedbloed, Hennie van der Meiden, and Egbert Westerhof of the FOM DIFFER institute for stimulating discussions on plasma confinement. This work is funded by NWO VICI 680-47-604 and NSF Grant No. PHY-1206118. C. B. S. was supported by the NWO Graduate Programme.

S. C. acknowledges financial support from the UKs STFC (Grant No. STK/K000993/1). We acknowledge support from the Casimir Research program Leiden-Delft and from NWO through a Spinoza prize.

[1] R. B. White, *The Theory of Toroidally Confined Plasmas* (Imperial College Press, London, 2001).
[2] R. D. Hazeltine and J. D. Meiss, *Plasma Confinement* (Dover Publications, Inc., Mineola, NY, 2003).
[3] A. E. Broderick and R. Narayan, Mon. Not. R. Astron. Soc. **383**, 943 (2008).
[4] J. Braithwaite, Mon. Not. R. Astron. Soc. **397**, 763 (2009).
[5] A. Brandenburg, Plasma Phys. Controlled Fusion **51**, 124043 (2009).
[6] B. L. Tan and G. L. Huang, Astron. Astrophys. **453**, 321 (2006).
[7] J. Braithwaite, Mon. Not. R. Astron. Soc. **406**, 705 (2010).
[8] B. C. Low, J. Geophys. Res. **106**, 25141 (2001).
[9] T. R. Jarboe, Plasma Phys. Controlled Fusion **36**, 945 (1994).
[10] M. Tuszewski, Nucl. Fusion **28**, 2033 (1988).
[11] P. Kubes, M. Paduch, T. Pisarczyk, M. Scholz, D. Klir, J. Kravarik, K. Rezac, T. Chodukowski, I. Ivanova-Stanik, L. Karpinski *et al.*, IEEE Trans. Plasma Sci. **38**, 672 (2010).
[12] J. Taylor, Phys. Rev. Lett. **33**, 1139 (1974).
[13] J. Cantarella, D. DeTurck, and H. Gluck, AMS/IP Studies In Advanced Mathematics **24**, 1 (2001).
[14] S. Hudson, E. Startsev, and E. Feibush, Phys. Plasmas **21**, 010705 (2014).
[15] G. E. Marsh, *Force-Free Magnetic Fields Solutions, Topology and Applications* (World Scientific, Singapore, 1996).
[16] L. Woltjer, Proc. Natl. Acad. Sci. U.S.A. **44**, 489 (1958).
[17] H. Moffatt, J. Fluid Mech. **35**, 117 (1969).
[18] A. M. Kamchatnov, Sov. Phys. JETP **55**, 69 (1982).
[19] A. Thompson, J. Swearngin, A. Wickes, and D. Bouwmeester, Phys. Rev. E **89**, 043104 (2014).
[20] M. A. Berger, Plasma Phys. Controlled Fusion **41**, B167 (1999).
[21] F. Del Sordo, S. Candelaresi, and A. Brandenburg, Phys. Rev. E **81**, 036401 (2010).
[22] Y. Ono, M. Inomoto, T. Okazaki, and Y. Ueda, Phys. Plasmas **4**, 1953 (1997).
[23] S. Candelaresi and A. Brandenburg, Phys. Rev. E **84**, 016406 (2011).
[24] A. Brandenburg and W. Dobler, Comput. Phys. Commun. **147**, 471 (2002).
[25] See Supplemental Material at http://link.aps.org/supplemental/10.1103/PhysRevLett.115.095001 for the equations solved in the simulation, additional descriptions of field dynamics, postprocessing of the simulation results and mathematical derivation of the analytical fields.
[26] S. Hudson, R. Dewar, G. Dennis, M. Hole, M. McGann, G. von Nessi, and S. Lazerson, Phys. Plasmas **19**, 112502 (2012).
[27] P. M. Bellan, *Fundamentals of Plasma Physics* (Cambridge University Press, Cambridge, 2006).
[28] R. M. Kulsrud, *Plasma Physics for Astrophysics* (Princeton University Press Princeton, 2005), Vol. 77.
[29] R. Fitzpatrick, Fusion Sci. Technol. **59**, 625 (2011).
[30] J. P. Goedbloed and S. Poedts, *Principles of Magnetohydrodynamics: With Applications to Laboratory and Astrophysical Plasmas* (Cambridge University Press, Cambridge, 2004).
[31] J. P. Goedbloed, R. Keppens, and S. Poedts, *Advanced Magnetohydrodynamics: With Applications to Laboratory and Astrophysical Plasmas* (Cambridge University Press, Cambridge, 2010).
[32] M. McGann, S. Hudson, R. Dewar, and G. Von Nessi, Phys. Lett. A **374**, 3308 (2010).
[33] H. Hopf, Math. Ann. **104**, 637 (1931).
[34] A. F. Rañada, Lett. Math. Phys. **18**, 97 (1989).
[35] A. Rañada and J. Trueba, Phys. Lett. A **202**, 337 (1995).
[36] R. Z. Sagdeev, S. S. Moiseev, A. V. Tur, and V. V. Yanovskii, in *Nonlinear Phenomena in Plasma Physics and Hydrodynamics* (Mir Publishers, Moscow, 1986), Vol. 1, pp. 137–182.
[37] M. Arrayás and J. L. Trueba, arXiv:1106.1122.